Imaging multiple Rydberg wave packets from shaper-generated two-color femtosecond pump-probe sequences

S. Kerbstadt, L. Gabrisch, K. Eickhoff, T. Bayer, and M. Wollenhaupt
Carl von Ossietzky Universität Oldenburg, Institut für Physik, Carl-von-Ossietzky-Straße 9-11, D-26129 Oldenburg, Germany

(Received 2 November 2018; published 7 January 2019)

We combine a bichromatic white light polarization pulse shaping scheme with angle- and energy-resolved photoelectron spectroscopy to image the dynamics of atomic Rydberg wave packets. Background-free detection of the Rydberg dynamics is performed using shaper-generated bichromatic linearly and circularly polarized femtosecond pump-probe pulse sequences. Photoelectron momentum distributions from linearly polarized bichromatic fields feature pronounced time-, energy-, and angle-dependent dynamics, which result from the interference of s-, d-, and g-type photoelectron wave packets from the ionization of the Rydberg np and nf series. Detailed analysis of the highly differential data allows us to extract the dynamics of both Rydberg wave packets separately. The results are experimentally verified by additional pump-probe studies with bichromatic circularly polarized pulse sequences, which exclusively map the dynamics of the Rydberg nf series via g-type photoelectron wave packets.

DOI: 10.1103/PhysRevA.99.013406

I. INTRODUCTION

Rydberg atoms are highly excited quantum systems typically generated by light pulses driving the electron from its initial ground state into the Rydberg series, i.e., into states with high principal quantum number n close to the ionization threshold [1]. Due to the dense spacing of the energy levels in the Rydberg series, an ultrashort laser pulse excites a coherent superposition of several Rydberg states and creates a bound Rydberg wave packet oscillating in the radial direction [2–5]. The unusual properties of Rydberg wave packets have been investigated both theoretically [3,4] and experimentally [5–8] for some time now. Recent applications of Rydberg atoms, such as data storage and retrieval [9,10] as well as Rydberg quantum simulators [11,12] underline the important role of Rydberg atoms in future technology. Optical pump-probe techniques are particularly suitable to probe the dynamics of Rydberg wave packets. In such experiments, the neutral Rydberg wave-packet dynamics are excited by a first pump pulse and probed by a time-delayed second pulse, for example by photoionization. By this means, the time evolution of the bound Rydberg wave packet is mapped on the photoionization signal and recorded by variation of the time delay. This approach was investigated on alkali atoms both theoretically [13] and experimentally [6,14,15]. Recently, the pump-probe technique has been refined to resolve attosecond dynamics by using an XUV pump pulse to excite bound Rydberg states and a time-delayed IR-pulse as probe pulse [16]. Technical progress in the generation of tailored ultrashort laser pulses also enables coherent control of Rydberg wave packets in atoms and molecules [2,14,17–20]. In this paper, we combine an advanced bichromatic femtosecond (fs) polarization pulse shaping scheme with angle- and energy-resolved photoelectron imaging techniques to map the dynamics of Rydberg wave packets from multiphoton excitation of potassium (K) atoms. For this purpose, we employ a bichromatic $4f$ white light polarization pulse shaper [21–23] to generate fully controlled and tunable phase-locked two-color fs pulse sequences. In the experiments, the center frequencies are chosen such that the pump pulse induces a 3-photon excitation of a bound Rydberg electron wave packet in the np and nf series ($n = 8, \ldots, 25$), which is probed by 1-photon ionization. Using bichromatic fields, the multiphoton ionization (MPI) pathway of the Rydberg signal is energetically separated from the single-color pathways involved in the pump and probe step [24], allowing background-free imaging of the Rydberg wave packet into a distinct kinetic energy window of the photoelectron spectrum. The pump-probe delay between the two colors was implemented with our high precision [25] pulse shaper by linear spectral phase modulation. For each time delay, a two-dimensional (2D) projection of the photoelectron momentum distribution is recorded using a velocity map imaging (VMI) spectrometer [26]. The energy- and angle-resolved detection permits a highly differential analysis of the induced Rydberg dynamics, which is demonstrated on a well-established atomic model system.

The paper is structured as follows. First, we present our experimental scheme for background-free angle- and energy-resolved detection of photoelectron momentum distributions from excited Rydberg wave packets in Sec. II A. The experimental strategy and the physical system are introduced in Sec. II B. The experimental results discussed in Sec. III are subdivided in three parts. First, we perform an energy-resolved analysis of photoelectron spectra from linearly polarized bichromatic fields to identify the kinetic energy window for the background-free detection of the Rydberg wave-packet dynamics. In the second part, we analyze the angle-resolved photoelectron spectra within this kinetic energy window. Two different methods for analysis are applied to separate the entangled Rydberg dynamics observed in the superposition of the s-, d-, and g-type photoelectron wave packets. In the first

method, we fit time-dependent amplitudes to model the experimental data, while in the second, we extract the dynamics directly from the angle-resolved experimental data at specific angles. In both cases, the beating frequencies are obtained by Fourier analysis to identify the involved Rydberg states within the np and nf series. In part three, both methods for analysis are verified experimentally by an additional pump-probe study using a corotating circularly polarized bichromatic pulse sequence to selectively excite the Rydberg nf series, which is probed exclusively into a g-type continuum. In Sec. IV, we conclude and give an outlook.

II. EXPERIMENT

A. Experimental scheme

In this section, we present the shaper-based bichromatic pump-probe scheme for background-free angle- and energy-resolved imaging of photoelectron momentum distributions from excited Rydberg wave packets. To this end, we combine a bichromatic $4f$ white light polarization pulse shaper [24] with a VMI spectrometer. In the experiments, we use a FEMTOLASERS multipass chirped pulse amplifier (Rainbow 500, Femtopower HR 3kHz, 0.8 mJ pulse energy) to seed a neon-filled hollow-core fiber (absolute gas pressure of 2.5 bar) for the generation of white light supercontinua (WLS). The WLS pulses are spectrally modulated using a home-built $4f$ polarization pulse shaper [22,27,28] specifically adapted to the ultra-broadband WLS [23]. Spectral phase and amplitude modulation of the WLS are realized with a dual-layer liquid crystal spatial light modulator (LC-SLM; *Jenoptik* SLM-640d) and a broadband p polarizer (*CODIXX* colorPol) positioned in the Fourier plane of the $4f$ setup. The polarizer is mounted behind the LC-SLM to sculpture horizontally polarized bichromatic amplitude profiles from the input WLS via combined amplitude and phase modulation [22,23], as depicted in Fig. 1(a). The shaper-generated bichromatic amplitude profile consists of two fully controlled spectrally separated bands with individually adjustable and tunable center frequencies $\omega_{1,2}$, amplitudes $\mathcal{A}_{1,2}(\omega)$, spectral widths $\Delta\omega_{1,2}$, spectral phases $\varphi_{1,2}(\omega)$ and polarizations. The center frequencies $\omega_1 = 2.125\,\mathrm{rad/fs}$ and $\omega_2 = 2.850\,\mathrm{rad/fs}$ are selected, as illustrated by the measured spectrum shown in Fig. 1(b). The spectral widths are chosen to be $\Delta\omega_1 = \Delta\omega_2 = 0.05\,\mathrm{rad/fs}$, corresponding to a pulse duration of $\Delta t_1 = \Delta t_2 = \Delta t \simeq 55\,\mathrm{fs}$. The pulse duration was verified by an *in situ* shaper-based cross-correlation (CC) measurement [see Fig. 1(c)] recorded by integrating the photoelectron yield from MPI of K atoms in the interaction region of the VMI spectrometer [21,23]. By additional use of a superachromatic quarter wave plate (*Bernhard Halle Nachfl. GmbH*, RSU 1.4.15, $\lambda = 300, \ldots, 1100\,\mathrm{nm}$) at the shaper output, the bichromatic polarization state is controlled to generate either parallel linearly polarized (PLP) or corotating circularly polarized (COCP) bichromatic pump-probe pulse sequences [22,23]. The shaper is also used for the temporal compression of the bichromatic fields. Residual spectral phases are compensated by shaper-based adaptive optimization of the second harmonic generation in a thin β-barium borate crystal (*GWU-Lasertechnik*, $\theta = 29.2^\circ$, 5-μm thickness) using an evolutionary algorithm [29,30]. Linear spectral phase modulation of the blue band with $\varphi_2(\omega) = \tau(\omega - \omega_2)$ temporally advances ($\tau > 0$) or delays ($\tau < 0$) the blue relatively to the red pulse to create phase-locked bichromatic pulse sequences for the two-color pump-probe experiments. Due to the common-path geometry of the bichromatic shaping scheme, inherent phase and mechanical stability are provided. Using a spherical mirror with a focal length of $f = 250\,\mathrm{mm}$, the bichromatic pulse sequences are focused (intensity $I \approx 10^{12}\,\mathrm{W/cm^2}$) into the interaction region of a VMI spectrometer. The VMI spectrometer is filled with K vapor supplied by a dispenser source (*SAES Getters*). Angle- and energy- resolved 2D projections of three-dimensional (3D) photoelectron momentum distributions from MPI of K atoms are imaged onto a position sensitive detector (*Scientific Instruments* S3075-10-I60-PS43-FM) consisting of a dual-layer multichannel-plate in chevron configuration followed by a phosphor screen. The 2D images are recorded by a charge coupled device camera (*Lumenera* LW165M) using an exposure time of 250 ms. Each projection is acquired by accumulation of 150 images. By automated variation of the time delay from $\tau = -100\,\mathrm{fs}$ (where the blue precedes the red pulse) to 1000 fs (where the blue follows the red pulse) using the pulse shaper and a step size of $\Delta\tau =$

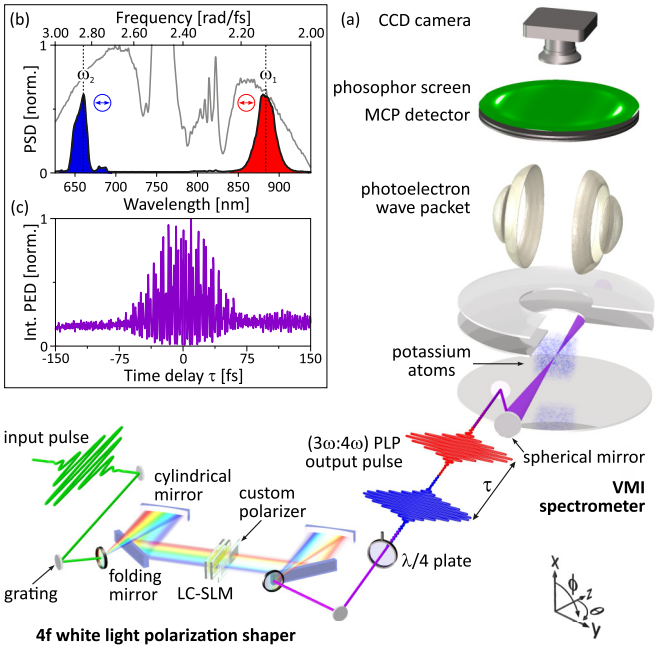

FIG. 1. (a) The experimental setup used for the pump-probe studies of Rydberg wave-packet dynamics in potassium atoms consists of a bichromatic $4f$ white light polarization pulse shaper and a VMI spectrometer. Shaper-generated bichromatic (3ω:4ω) PLP pulse sequences with variable time delay τ are focused into potassium vapor in the interaction region of the VMI spectrometer. Photoelectron wave packets from 3-photon excitation (pump) and time-delayed ionization (probe) are imaged onto the 2D detector and recorded as a function of τ. Inset (b) shows the measured bichromatic amplitude profile (red and blue shaded) together with the white light input spectrum (gray line). Inset (c) depicts a shaper-based *in situ* bichromatic cross-correlation trace [21] obtained by integrating the photoelectron yield from MPI of K atoms.

10 fs, 111 2D projections of photoelectron wave packets are measured, mapping the time evolution of Rydberg wave packets. The detected 2D projections of the photoelectron momentum distributions are Abel-inverted using the pBASEX algorithm [31] and energy-calibrated [32] to retrieve the 3D density and extract equatorial sections (within the z-y plane) through the generated photoelectron wave packets [see, for example, Figs. 2(b) to 2(d)]. A retrieved 3D photoelectron wave packet from multiple excited Rydberg states (at $\tau = 360$ fs) is shown in Fig. 1(a). To highlight photoelectron wave packets from the Rydberg states, the single-color contributions are suppressed.

B. Physical system and experimental strategy

In this section, we introduce the physical system and describe our experimental strategy to excite and probe the dynamics of Rydberg wave packets. The pump-probe scheme for two-color excitation and ionization of K atoms by bichromatic PLP fields is depicted in Fig. 2(a). Rydberg wave-packet dynamics are initialized in the nf and np series via 3-photon excitation by the pump pulse centered around $\omega_1 = 2.125$ rad/fs (referred to as red pulse). The relevant quantum pathways are indicated by red arrows in Fig. 2(a). The np series is excited by two pathways via the intermediate $5s$ and $3d$ resonances, whereas the nf series is excited exclusively by the pathway via the $3d$ resonance. Owing to the spectral width of the red pump pulse, the Rydberg states $8f, \ldots, 24f$ and $9p, \ldots, 25p$ are covered by the third-order spectrum, as visualized in the inset to Fig. 2(a). However, due to the intermediate resonances and Stark shifts during the excitation, the population distribution among those states is not only determined by the third-order power spectral density, see, for example, [33].

The time-dependent wave function of the excited Rydberg wave packets is described by the superposition [1,6,34]

$$\psi(r,\vartheta,t) = \sum_{n}^{N} \psi_{p,n}(r,\vartheta) e^{-i\omega_n t} + \sum_{j}^{J} \psi_{f,j}(r,\vartheta) e^{-i\omega_j t}. \quad (1)$$

The wave functions on the right-hand side are given by $\psi_{p,n}(r,\vartheta) = p_n R_{p,n}(r) Y_{10}(\vartheta)$ and $\psi_{f,j}(r,\vartheta) = f_j R_{f,j}(r) Y_{30}(\vartheta)$, with radial parts $R_{p,n/j}(r)$ and spherical harmonics $Y_{\ell 0}(\vartheta)$. The auxiliary angle ϑ is introduced to simplify the notation. It is the polar angle of a coordinate frame with z axis aligned in the laser polarization direction (current y direction; see Fig. 2). This allows us to express the excited state wave function from linearly polarized excitation in terms of spherical harmonics with $m = 0$ [24,35]. The population amplitudes p_n and f_j result from 3-photon excitation of Rydberg np and nf states, respectively, and are time-independent after the interaction with the pump pulse (interaction picture). The frequencies ω_n and ω_j are the eigenfrequencies of the related Rydberg states. The corresponding electron density can be decomposed into oscillatory functions with frequencies $\omega_{lk} \equiv \omega_l - \omega_k$ and is described by

$$|\psi(t)|^2 \propto \sum_{n}^{N} |\psi_{p,n}|^2 + \sum_{j}^{J} |\psi_{f,j}|^2 + 2\mathrm{Re}\left\{ \sum_{\substack{n,m \\ n<m}}^{N} \psi_{p,n}\psi_{p,m}^* e^{i\omega_{mn}t} + \sum_{\substack{j,k \\ j<k}}^{J} \psi_{f,j}\psi_{f,k}^* e^{i\omega_{kj}t} \right\}$$
$$+ \sum_{n,k}^{N,J} \psi_{p,n}\psi_{f,k}^* e^{i\omega_{kn}t} + \sum_{j,m}^{J,N} \psi_{f,j}\psi_{p,m}^* e^{i\omega_{mj}t}, \quad (2)$$

with Re denoting the real part of the wave functions.

The first two sums in the brackets describe intraseries quantum beatings within the nf and the np series, respectively. The last two sums correspond to interseries beatings between states from both the np and the nf series.

The Rydberg dynamics are probed via 1-photon ionization by the time-delayed pulse centered around $\omega_2 = 2.850$ rad/fs (referred to as blue pulse). Due to the dipole selection rules, the p-type Rydberg wave packet is mapped onto s- and d-type ionization continua, whereas the f-type Rydberg wave packet is probed into d- and g-type ionization continua. To describe the created photoelectron wave packets, we employ first-order time-dependent perturbation theory. For example, consider ionization from state $\psi_{p,n}$ to the d-type continuum. Denoting the electric field of the probe pulse in time and frequency domain by $E_{pr}(t)$ and $\tilde{E}_{pr}(\omega)$, respectively, and applying the Fourier shift theorem, the momentum space (k) wave function of the photoelectron wave packet created at the time delay τ is obtained as

$$\psi_{d\leftarrow p,n}(k,\vartheta,\tau) = \frac{\mu_{kn}^{dp}\, p_n}{i\hbar} \int_{-\infty}^{\infty} E_{pr}(t-\tau)\, e^{i(\omega_k-\omega_n)t} dt\, Y_{20}(\vartheta) = \frac{\mu_{kn}^{dp}\, p_n}{i\hbar}\, \tilde{E}_{pr}(-\omega_{kn})\, e^{i\omega_{kn}\tau}\, Y_{20}(\vartheta) = d_{p,n}(k)\, e^{-i\omega_n\tau}\, Y_{20}(\vartheta). \quad (3)$$

Herein, μ_{kn}^{dp} is the corresponding radial transition dipole moment and $d_{p,n}(k)$ incorporates the k-dependent part of the photoelectron wave function. The total photoelectron wave function is composed of four contributions calculated analogously:

$$\psi(k,\vartheta,\tau) = \sum_{n}^{N} s_{p,n}(k)\, e^{-i\omega_n\tau}\, Y_{00}(\vartheta) + \sum_{n,j}^{N,J} [d_{p,n}(k)\, e^{-i\omega_n\tau} + d_{f,j}(k)\, e^{-i\omega_j\tau}] Y_{20}(\vartheta) + \sum_{j}^{J} g_{f,j}(k)\, e^{-i\omega_j\tau}\, Y_{40}(\vartheta). \quad (4)$$

The s-type photoelectron wave packet in the first row exclusively maps the intraseries beatings within the Rydberg np series, whereas the g-type photoelectron wave packet in the third row exclusively reflects intraseries beatings within the Rydberg nf series. In contrast, the d-type photoelectron wave packet in the second row results from the interference of contributions from both Rydberg series, mapping the interseries beatings between the Rydberg np and nf states in addition.

The commensurable center frequencies $\omega_2 \approx \frac{4}{3}\omega_1$ of the pump and probe pulse permit background-free detection of the Rydberg dynamics in a kinetic energy window centered around $\varepsilon_R = 3\hbar\omega_1 + 1\hbar\omega_2 - V_{\text{ion}} \approx 1.73\,\text{eV}$. The single-color contributions are energetically separated from the probed Rydberg signal and overlap around $\varepsilon_S = 4\hbar\omega_1 - V_{\text{ion}} \approx 3\hbar\omega_2 - V_{\text{ion}} \approx 1.27\,\text{eV}$. Here $V_{\text{ion}} \approx 4.34\,\text{eV}$ denotes the ionization potential of the K atom. Direct 4-photon ionization by the pump pulse launches photoelectron wave packets in s-, d-, and g-type ionization continua. The probe pulse gives rise to photoelectron wave packets with p- and f-type symmetry via 3-photon ionization. Both the red pump and the blue probe pulse are chosen to be nonresonant with the atomic $4p \leftarrow 4s$ transition.

To illustrate our experimental strategy, Figs. 2(b) to 2(d) display Abel-inverted and energy-calibrated equatorial sections through photoelectron wave packets, measured for three characteristic time delays τ between the pump and probe pulse. For $\tau = -260\,\text{fs}$ [Fig. 2(b)], the probe pulse precedes the pump pulse. Hence no Rydberg wave packets are excited and only a superposition of energetically overlapping f- and g-type photoelectron wave packets from single-color MPI by both pulses is observed at ε_S. At $\tau = 0\,\text{fs}$ [Fig. 2(c)], three additional f-type photoelectron wave packets from third-order intrapulse frequency-mixing of the temporally overlapping pump and probe pulses emerge [24]. This includes the Rydberg wave packet probed at ε_R and two low-energy contributions at $\varepsilon_3 = 2\hbar\omega_1 + 1\hbar\omega_2 - V_{\text{ion}} \approx 0.34\,\text{eV}$ and $\varepsilon_4 = 1\hbar\omega_1 + 2\hbar\omega_2 - V_{\text{ion}} \approx 0.81\,\text{eV}$. For $\tau = +260\,\text{fs}$ [Fig. 2(d)], the probe follows the pump pulse. The single-color contributions at ε_S and a pronounced contribution of the ionized Rydberg wave packet at ε_R remain.

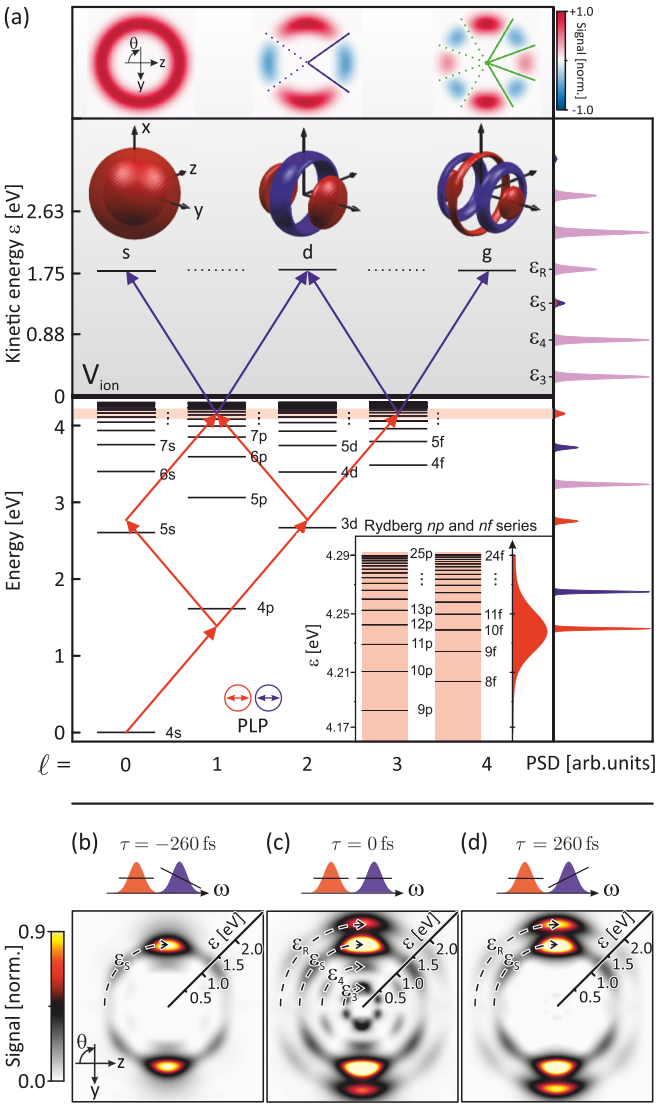

FIG. 2. (a) Excitation scheme for K atoms interacting with a bichromatic (3ω:4ω) PLP pulse sequence. The pump pulse (red arrows) launches Rydberg wave packets in the np and nf series via 3-photon excitation. Time-delayed 1-photon ionization by the probe pulse (blue arrows) maps the Rydberg dynamics onto s-, d-, and g-type ionization continua. The corresponding photoelectron wave packets (calculated) and their equatorial sections are illustrated on top. The sign of the wave functions is color-coded in red (+) and blue (−). The right panel displays nonlinear optical spectra up to fourth order to indicate the different channels from single-color excitation (red and blue) and frequency mixing (magenta). The inset shows a magnification of the two Rydberg series covered by the measured third-order spectrum of the pump pulse. (b)–(d): Selected measured and energy-calibrated equatorial y-z sections through photoelectron momentum distributions at (b) $\tau = -260\,\text{fs}$, (c) $\tau = 0\,\text{fs}$, and (d) $\tau = +260\,\text{fs}$.

III. RESULTS AND DISCUSSION

In this section, the experimental results of our pump-probe studies on Rydberg wave-packet dynamics, excited and probed using bichromatic PLP and COCP fields, are presented and discussed. To identify a suitable spectral band in the photoelectron kinetic energy distribution for the observation of the Rydberg dynamics, we perform an energy-resolved (i.e., angle-integrated) analysis. By integration over the polar angle $\theta \in [0, 360]^\circ$, one-dimensional (1D) photoelectron spectra are obtained from the recorded 2D VMI images and plotted as a function of the time delay τ in Fig. 3. The results are presented in Fig. 3(a), together with a section along the τ axis (τ section) taken at $\varepsilon_R \approx 1.73\,\text{eV}$ in Fig. 3(b) and the corresponding Fourier spectrum in Fig. 3(c). The signals from single-color MPI at $\varepsilon_S \approx 1.27\,\text{eV}$ remain essentially constant for all time delays. For $\tau \lesssim -\Delta t$, no photoionization signal from the Rydberg wave packets is detected. Within the temporal pulse overlap window, i.e., $|\tau| \lesssim \Delta t$, the three distinct contributions from intrapulse frequency-mixing [24] arise (cf. Fig. 2), including the probed Rydberg electron wave packet around $\varepsilon_R \approx 1.73\,\text{eV}$. The contribution at ε_3 indicates a Stark shift during the temporal overlap and also remains for $\tau > \Delta t$ because of the involved intermediate resonances $3d$ and $5s$ addressed via two red photons during the pump step

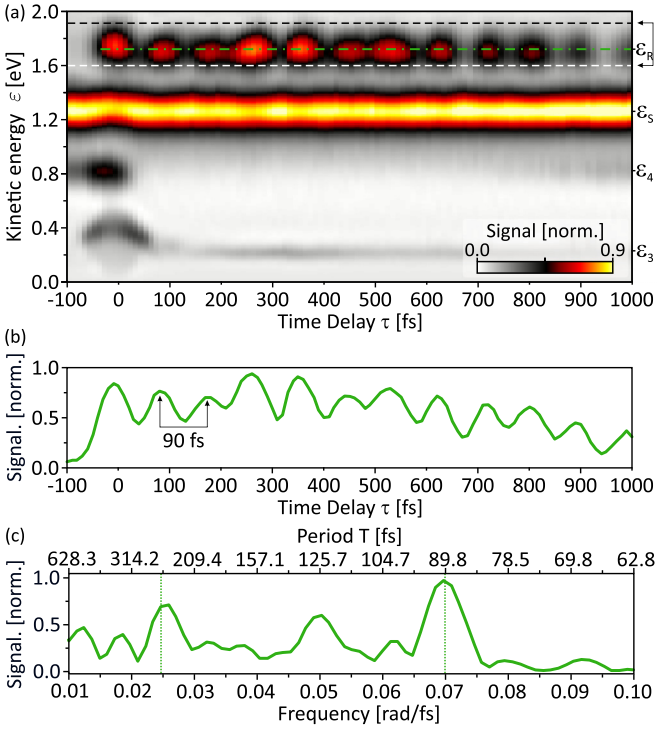

FIG. 3. (a) Kinetic energy-resolved photoelectron spectra generated by excitation and ionization of K atoms with bichromatic PLP pump-probe pulse sequences as a function of the time delay τ. The spectra were obtained by integrating the measured 2D VMI images over the polar angle $\theta \in [0, 360]^\circ$. The Rydberg wave packet dynamics induced by the pump pulse are mapped into the energy window around $\varepsilon_R \approx 1.73$ eV by the probe. (b) Section through (a) along the time axis at ε_R marked by the green dash-dotted line. The prominent oscillation with a period of $T \approx 90$ fs corresponds to the pronounced frequency component observed at $\omega = 0.07$ rad/fs in the Fourier spectrum in (c).

[cf. Fig. 2(a)]. As soon as the pump and probe pulse are temporally separated, i.e., for $\tau \gtrsim \Delta t$, the contribution from nonresonant frequency-mixing at ε_4 vanishes, whereas the contribution at ε_3 and the Rydberg signal at ε_R persist. Due to the excitation of multiple Rydberg states by the red pump pulse [see inset to Fig. 2(a)], a pronounced oscillation of the photoelectron yield is observed in the kinetic energy window around $\varepsilon \in [1.6, 1.9]$ eV [white and black dashed lines in Fig. 3(a)]. The section through the data taken at 1.73eV [Fig. 3(b)] reveals a principal oscillation with a period of $T \approx 90$ fs. This is confirmed by the Fourier spectrum shown in Fig. 3(c), which is dominated by the component centered at $\omega \approx 0.07$ rad/fs.

Further details of Rydberg wave-packet dynamics are revealed by analysis of the angle-resolved photoelectron distribution within the relevant kinetic energy window $\varepsilon \in [1.6, 1.9]$ eV around ε_R (see white and black dashed lines in Fig. 3). For this purpose, polar angle θ-resolved photoelectron distributions are obtained by integrating the Abel-inverted 2D VMI images over the relevant photoelectron kinetic energy interval. In Fig. 4, the resulting θ-resolved photoelectron distributions are plotted as a function of the time delay τ. The angular interval $\theta \in [120, 240]^\circ$ is displayed in Fig. 4(b) using a different color scale to emphasize small contributions. Vertical sections through the data in Figs. 4(a) and 4(b) along the time axis are shown in Fig. 4(c), together with the corresponding Fourier spectra in Fig. 4(d). Horizontal sections taken along the θ axis are presented in Fig. 4(e) and compared to the results from a fitting model described below. In addition to the prevailing oscillation with a period $T \approx 90$ fs, already observed in Fig. 3, low-frequency oscillations with a period of $T \approx 260$ fs appear in the angular dynamics of the equatorial lobes of the photoelectron wave packets. This slow oscillation is best discernible in Fig. 4(b) at $\theta = 160^\circ$ and $\theta = 180^\circ$, the corresponding τ sections are plotted in Fig. 4(c) as red dashed and solid green lines. The observed angular dynamics of the photoelectron density in this region result from the interference of s-, d-, and g-type wave packets. As will be shown below, the dynamics are mainly caused by a variation of the d-type wave packet. Because of the different (polar) nodal structure of the individual contributions [cf. Fig. 2(a)] and, in addition, the different time evolutions of the underlying Rydberg wave packets, the interference character changes both with the angle θ and with the time delay τ. Figure 4(e) shows two angle-resolved photoelectron spectra at distinctive time delays. At $\tau = 90$ fs, we observe an almost pure g-type angular distribution characterized by two main and three side lobes. For $\tau = 260$ fs, however, the angular distribution is altered significantly. The central side lobe has vanished due to destructive interference between the g- and the d-type wave packet. The remaining two side lobes are slightly shifted towards the equator ($\theta = 180^\circ$). Since both wave packets are in antiphase around the equator but exhibit a different number of nodes, they are in-phase around the two poles ($\theta = 90^\circ$ and 270°). Therefore, the amplitude of the two main lobes is enhanced by constructive interference between the g- and the d-type wave packet at this time delay. Both angular distributions recur with a period of $T = 260$ fs, visible in Fig. 4(b) and quantified by the τ-resolved sections at $\theta = 180^\circ$ and 160° plotted in Fig. 4(c). The Fourier spectra of both sections, shown in Fig. 4(d), are dominated by the slow $T \approx 260$ fs component at $\omega = 0.024$ rad/fs, whereas the fast $T \approx 90$ fs component at $\omega = 0.07$ rad/fs is slightly suppressed. The Fourier spectrum of the section at $\theta = 90^\circ$ is very similar to the angle-integrated result shown in Fig. 3(c) since the major part of the electron density is contained in the main lobes. The pronounced angular dynamics by interference of wave functions with the same parity is an example for phase control over the differential photoionization cross section, as pointed out in [37].

Because the detected photoelectron momentum distributions originate from interfering s-, d-, and g-type electron wave packets, it is difficult to infer the Rydberg dynamics in the np and nf series from the measurements separately. In the following, we employ two methods to separate the dynamics of the s-, d-, and g-type electron wave packets. In one approach, we fit the probability density of a superposition of s-, d-, and g-type wave functions according to Eq. (4)

$$\rho(\vartheta, \tau) = |\psi_s(\vartheta, \tau) + \psi_d(\vartheta, \tau) + \psi_g(\vartheta, \tau)|^2 = \left| \sum_{n=0}^{2} a_n(\tau)\, e^{i\phi_n(\tau)}\, Y_{2n,0}(\vartheta) \right|^2 \quad (5)$$

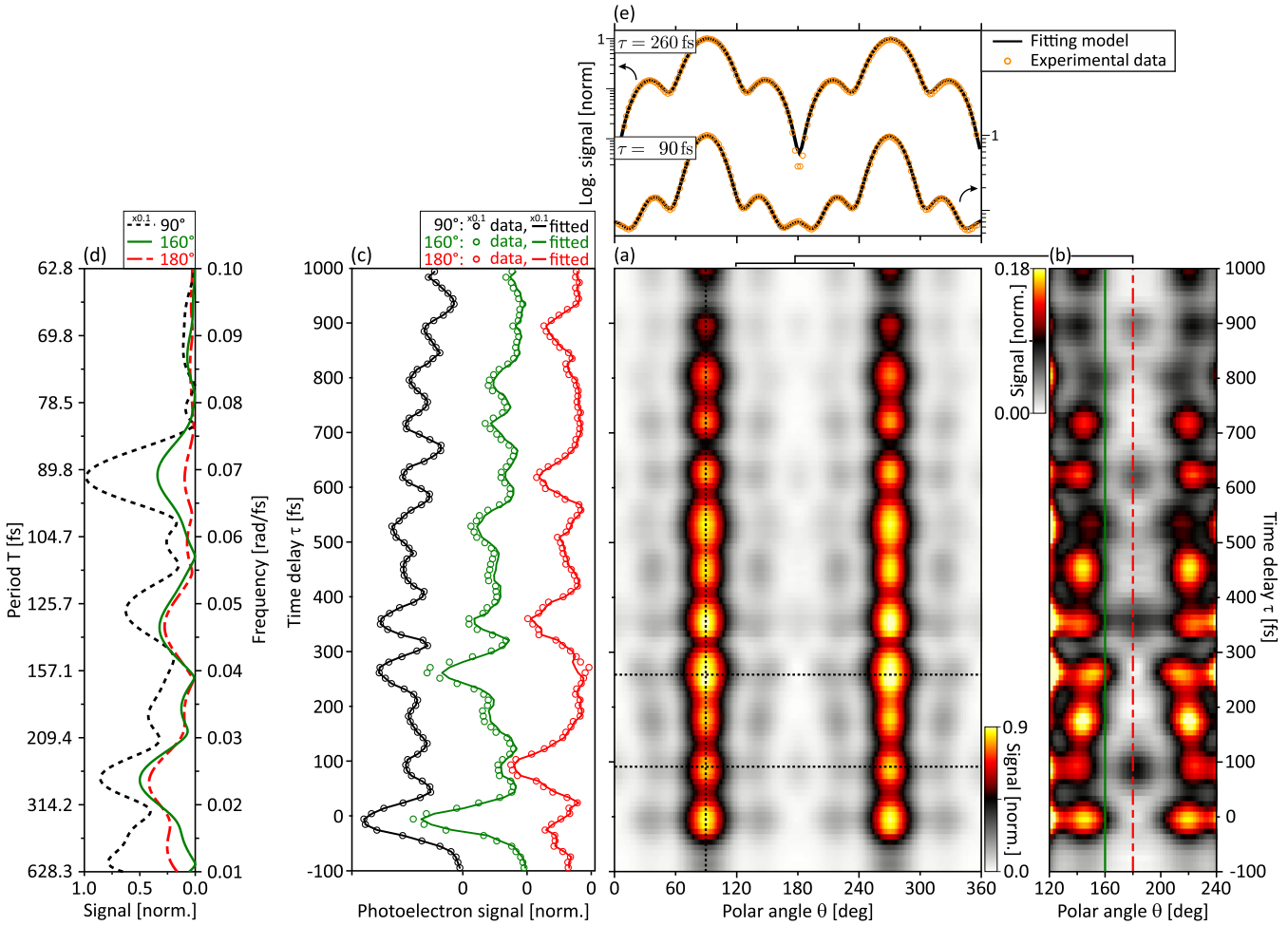

FIG. 4. (a) Time- and angle-resolved photoelectron momentum distributions in the energy window around $\varepsilon_R \approx 1.73$ eV measured using shaper-generated bichromatic PLP pump-probe pulse sequences. (b) A magnification of the interval $\theta \in [120, 240]^\circ$ to highlight the angular dynamics due to the interference of s-, d-, and g-type photoelectron wave packets is shown. (c) Sections through (a) taken along the τ axis at $\theta = 90^\circ$ (black circle), $\theta = 160^\circ$ (green circles), and $\theta = 180^\circ$ (red circles), together with the respective fits (solid lines) according to Eq. (5). The corresponding Fourier spectra of the experimental data are shown in (d). (e) Sections through (a) taken along the θ axis at $\tau = 90$ fs (lower plot) and at $\tau = 260$ fs (upper plot) in logarithmic representation (orange circles), along with fits (black solid lines).

to the measured photoelectron angular distribution using the real valued time-dependent amplitudes $a_{n=s,d,g}(\tau)$ for the s-, d-, and g-type wave functions. The phases accumulated in the excitation and ionization process, due to the phases of bound-free transition matrix elements [38] and Stark-shifts induced by the intermediate resonances, along with the subsequent time evolution are taken into account by the relative phases $\phi_{n=s,d,g}(\tau)$. A minor contribution to these phases may originate from partially incoherent superposition of the wave functions. However, previous results confirm the high degree of coherence in our experiments [21]. The results of the fitting procedure are exemplified in the logarithmic plot of two curves $\rho(\vartheta, \tau)$ (black solid lines) at characteristic delays $\tau = 90$ fs and $\tau = 260$ fs shown in Fig. 4(e). Comparison to the measured θ sections (orange circles) shows almost perfect agreement. By this means, we extract the amplitudes of s-, d-, and g-type wave packets for each time delay τ. In Figs. 5(a) to 5(c), the fitted time-dependent densities of s-, d-, and g-type wave packets are presented, along with their Fourier spectra in Figs. 5(e) to 5(g). To identify beatings between pairs of Rydberg states, as described in Eq. (2), line spectra indicating intraseries and interseries Rydberg modes are plotted in addition. To compare the fitted spectra $|\tilde{\psi}_{n=s,d,g}(\omega)|^2$ with the calculated line positions shown in Figs. 5(e) to 5(g), we consider the states of the Rydberg nf series for $|\tilde{\psi}_g(\omega)|^2$, the Rydberg np series for $|\tilde{\psi}_s(\omega)|^2$ and both Rydberg series for $|\tilde{\psi}_d(\omega)|^2$. In nonresonant excitation, the amplitudes of the lines are essentially described by the 3-photon power spectral density (PSD) of the pump pulse shown in Fig. 2. To qualitatively reproduce the effects of resonant excitation (via the $5s$ and $3d$ state), we introduce a slight red-shift of the PSD. The calculated line spectra are in reasonable agreement with the extracted spectra. Based on these results, we are able to analyze the Rydberg p and f dynamics separately and to identify the contributing states in the np and nf series (see Table I).

The second method to disentangle the contributions from d- and g-type wave packets is based on an angle-selective analysis of the measured data shown in Figs. 4(b) and 4(c).

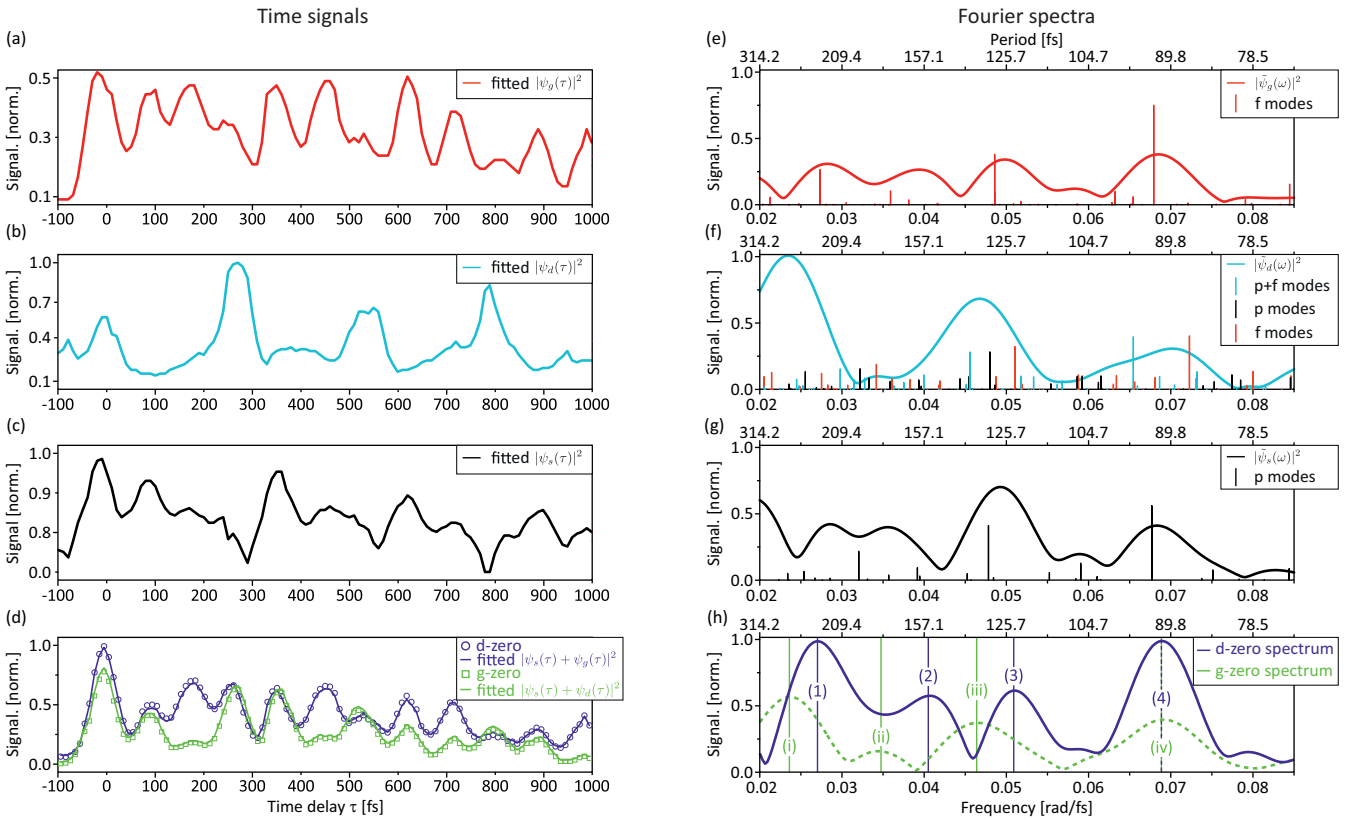

FIG. 5. (a)–(c) Time evolution of $|\psi_g(\tau)|^2$, $|\psi_d(\tau)|^2$ and $|\psi_s(\tau)|^2$ obtained by fitting the model described in Eq. (5) to the measured data. (d) Sections through the experimental data along the time axis at the zero-crossing of the g-type wave function ($\theta = 160.1^\circ$; green squares) and the d-type wave function ($\theta = 144.7^\circ$; blue circles). The experimental curves are compared to the fitting model $|\psi_s(\vartheta,\tau)+\psi_g(\vartheta,\tau)|^2$ (blue solid line) and $|\psi_s(\vartheta,\tau)+\psi_d(\vartheta,\tau)|^2$ (green solid line). (e)–(h) The corresponding Fourier spectra together with calculated spectral lines of the respective Rydberg modes are shown. The calculations are based on the measured third-order optical spectrum of the pump pulse, taking spectral shifts due to intermediate resonances into account, and spectroscopic data taken from [36]. (e) The Fourier components of $|\tilde{\psi}_g(\omega)|^2$ are attributed to intra-series beatings within the Rydberg nf series only. (f) The spectrum $|\tilde{\psi}_d(\omega)|^2$ maps intra- as well as inter-series beatings between states from the Rydberg np and nf series. (g) The spectrum $|\tilde{\psi}_s(\omega)|^2$ exclusively maps intra-series beatings within the Rydberg np series. (h) Fourier spectra of the experimental sections in (d). The identified modes labeled by (i)–(iv) and (1)–(4) are listed in Table I.

We distinguish between the d- and g-type wave packets by extracting τ sections through the measured data [Fig. 4(a)] at polar angles θ, where either the d- or the g-type wave packet's contribution vanishes, i.e., at the zero-crossings of the associated Legendre polynomials $P_{\ell,0}$, with $\ell = 2, 4$, respectively. The polar zero-crossings of the d type (d zeros)

TABLE I. Overview of the experimentally determined Rydberg modes (first column) extracted from the spectra depicted in Fig. 4(c). The corresponding frequencies and oscillation periods are given in the second and third columns. The fourth column contains the assigned Rydberg states and the fifth column provides the theoretical frequencies based on spectroscopic data from the NIST data base [36]. Modes (i) to (iv) were obtained by evaluating the τ section taken at $\theta = 160.1^\circ$, i.e., the zero-crossing of g-type wave function. Modes (1) to (4) were derived from the τ sections at $\theta = 144.7^\circ$, where the d-type wave function exhibits a zero.

Mode	Frequency exp. [mrad/fs]	Period exp. [fs]	Rydberg states	Frequency theo. [mrad/fs]
(i)	≃24.0	≃261.8	$12p-11f$	24.4
(ii)	≃34.5	≃182.1	$12p-13p$	33.1
(iii)	≃46.0	≃136.6	$13p-15p$	45.2
(iv)	≃69.2	≃90.8	$14p-19p$ $16p-11f$ $11p-11f$	67.7 69.8 69.7
(1)	≃27.2	≃231.0	$11f-12f$	27.3
(2)	≃ 41.0	≃153.2	$16p-12f$	42.5
(3)	≃51.3	≃122.5	$12p-12f$	51.6
(4)	≃69.2	≃90.8	$8f-9f$ $16p-11f$ $11p-11f$	68.0 69.8 68.7

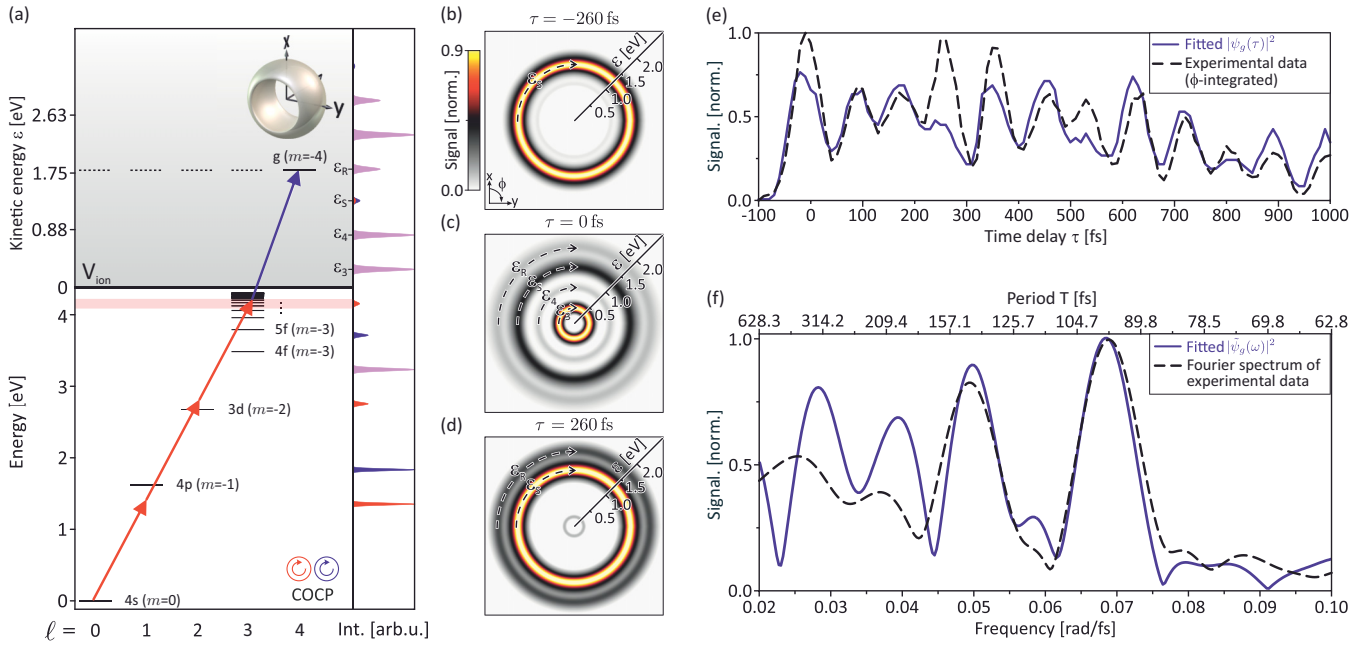

FIG. 6. Experimental results from the pump-probe measurement using (3ω:4ω) bichromatic COCP pulse sequences with otherwise same optical parameters as in the PLP scenario. (a) The excitation scheme for K atoms interacting with an RCP-RCP sequence is shown. Circularly polarized excitation by the RCP pump pulseleads to the selective population of the Rydberg nf series with $m = -3$. The RCP probe pulse maps the f-type Rydberg wave packet exclusively onto a g-type ionization continuum. (b)–(d) Selected x-y sections through the measured photoelectron momentum distributions at the characteristic time delays (b) $\tau = -260$ fs, (c) $\tau = 0$ fs, and (d) $\tau = 260$ fs identified in the PLP case. (e) Angle- (ϕ) and energy-integrated photoelectron signal from the Rydberg states as a function of the time delay τ. The experimental data (black dashed line) are compared to $|\psi_g(\tau)|^2$ of the g-type wave packet obtained by the fitting model in the PLP case (blue solid curve) [cf. Fig. 4(a)]. The corresponding Fourier spectra are displayed in (f).

and the g-type (g-zeros) photoelectron wave packets are illustrated in the top row of Fig. 2. The g zeros are found at the polar angles $\theta = 160.1°, 199.9°, 120.6°, 239.4°$ and the d zeros are located at $\theta = 144.7°, 215.3°$. Figure 5(d) shows τ sections of the g zero at $\theta = 160.1°$ (green rectangles) and the d zero at $\theta = 144.7°$ (blue circles). Comparison of the τ sections with the respective results from the fitting model $|\psi_s(\vartheta,\tau) + \psi_d(\vartheta,\tau)|^2$ and $|\psi_s(\vartheta,\tau) + \psi_g(\vartheta,\tau)|^2$ according to Eq. (5) shows excellent agreement. The corresponding Fourier spectra are depicted in Fig. 5(h) for both the measured d zeros (blue solid lines) and the g zeros (green dotted lines). The large Fourier component at $\omega \approx 69.2$ mrad/fs appears in both spectra and corresponds to the prominent $T \approx 90$ fs oscillation already visible in Figs. 3 and 4(a). This mode, labeled by (iv), originates from multiple quantum beats, e.g., between the states $14p - 19p$, $8f - 9f$, $16p - 11f$, and $11p - 11f$. Both spectra feature distinct additional peaks. All components are assigned to pairs of excited Rydberg states, based on spectroscopic data taken from [36], and listed in Table I.

We start with the analysis of the Fourier spectrum (green dotted line) of the g zeros shown in Fig. 5(h). The Fourier spectrum features similar modes as the spectra $|\tilde{\psi}_d(\omega)|^2$ and $|\tilde{\psi}_s(\omega)|^2$ obtained by the fitting procedure shown in Figs. 5(f) and 5(g), respectively. This observation confirms that in the angular segment around the g zeros, mainly the d- and s-type photoelectron wave packets contribute to the measured Fourier spectrum, mapping the dynamics of both the Rydberg np and nf series. The modes (ii) and (iii) correspond to beatings within the Rydberg np series, i.e., $12p - 13p$ (ii) and $13p - 15p$ (iii). The main mode (i) at $\omega = 0.024$ rad/fs is identified as the interseries beating $12p - 11f$. This mode corresponds to the low-frequency $T \approx 260$ fs oscillation associated with the angle-dependent dynamics observed in Fig. 4(a) around $\theta = 180°$. In the fitted data, the mode (i) is only visible in the Fourier spectrum $|\tilde{\psi}_d(\omega)|^2$ in Fig. 5(f). Hence, the angle-selective analysis reveals that the low-frequency angular dynamics in Fig. 4(b) are essentially determined by the d-type electron wave packet dynamics resulting from interseries beatings. The oscillation with a period of $T \approx 260$ fs appears most pronounced in the equatorial section through the measured data in Fig. 4(b) [see red dashed line in Fig. 4(c)].We continue with the discussion of the Fourier spectrum (blue solid line) of the d zeros, presented in Fig. 5(h). This allows us to analyze the Rydberg dynamics in the np and nf series, which are mapped onto the s- and g-type photoelectron wave packets, respectively. Interferences of s- and g-type photoelectron wave packets cause a quantum beat between the Rydberg np and nf series, leading to new beating frequencies that are not observed in the np or nf series alone. The Fourier spectra $|\tilde{\psi}_g(\omega)|^2$ and $|\tilde{\psi}_s(\omega)|^2$ in Figs. 5(e) and 5(g) show the same modes as those in the d-zero Fourier spectrum. The major frequency components (1)–(4) in the d-zero Fourier spectrum, displayed in Fig. 5(h),

are summarized in Table I. Mode (1) originates from the intraseries quantum beating of the states $11f - 12f$, whereas the frequency components (2)–(4) are due to interseries beatings of the states $16p - 12f$ [mode (2)], $12p - 12f$ [mode (3)], and $8f - 9f$, $16p - 11f$, $11p - 11f$ [mode (4)]. The analysis of the angle-resolved photoelectron spectra shows that we can elucidate the dynamics of multiple Rydberg wave packets, even in the presence of interfering continua.

To confirm the angle-selective analysis of the Rydberg wave-packet dynamics presented above, we performed an additional pump-probe experiment employing bichromatic COCP pulse sequences. Due to the dipole selection rules, COCP pulse sequences selectively excite the Rydberg nf series and map the Rydberg dynamics exclusively onto the g-type ionization continuum. The entailing suppression of the np series allows us to verify the above analysis of the energy- and angle-resolved photoelectron distributions. We use right-handed circularly polarized (RCP) pump and probe pulses which drive $\Delta m = -1$ transitions, implying a continuous increase of the orbital angular momentum ($\Delta\ell = +1$) and precluding $\Delta\ell = -1$ transitions. Energy-calibrated x-y sections through measured photoelectron momentum distributions obtained by bichromatic COCP pulse sequences are shown in Figs. 6(b) to 6(d) for three characteristic time delays. At $\tau = -260$ fs, when the probe pulse precedes the pump pulse, we observe only the single-color torus-shaped contribution at ε_S, but no probe signal from the Rydberg states. Setting $\tau = 0$ fs gives rise to further contributions from intrapulse frequency-mixing at $\varepsilon_{3,4}$ and from the probed Rydberg wave packet at ε_R. At $\tau = 260$ fs, Rydberg wave packets from the nf series are probed into a kinetic energy window around ε_R. The time-resolved angle-integrated (ϕ) signal within this energy window is shown in Fig. 6(e) (black dashed line), along with $|\psi_g(\tau)|^2$ obtained by the fitting model in the PLP case (blue solid line) [cf. Fig. 4(a)]. The corresponding Fourier spectra are depicted in Fig. 6(f). Both the time signals as well as the Fourier spectra are in good agreement, confirming the validity of the angle-selective analysis.

IV. CONCLUSION AND OUTLOOK

In this paper, we combine an advanced bichromatic white light polarization pulse shaping scheme [22,23] with energy- and angle-resolved imaging of photoelectron momentum distributions to map the dynamics of multiple excited Rydberg wave packets. Using a $4f$ polarization pulse shaper, we generate bichromatic phase-locked double pulse sequences with variable time delay for pump-probe studies of Rydberg wave packets from multiphoton ionization (MPI) of potassium (K) atoms. The bichromatic approach provided background-free detection of the Rydberg dynamics in a distinct kinetic energy window by energetic separation from the multiphoton quantum pathways involved in the pump and probe step. To analyze the different contributions, we employ either parallel linearly polarized (PLP) or corotating circularly polarized (COCP) bichromatic pulse sequences. In the case of PLP fields, Rydberg states of both the np and the nf series were populated by 3-photon excitation with the red pump pulse and mapped onto the s-, d-, and g-type continua via 1-photon ionization by the blue probe pulse. Interference of the s-, d-, and g-type photoelectron wave packets led to pronounced angle-dependent dynamics of the measured photoelectron momentum distributions. We analyze the time-dependent angle-resolved photoelectron momentum distributions to reveal the underlying Rydberg dynamics. In particular, we identified pairs of Rydberg states within the nf and np series that led to the prominent frequency contributions in the corresponding Fourier spectra. For this purpose, we employ two methods to separate the entangled Rydberg dynamics: the first method was based on a physical model describing the superposition of the s-, d-, and g-type photoelectron wave packets. The time-dependent amplitudes of the superposition were fitted to the experimental data. In the second approach, we extract the Rydberg dynamics directly from the measured data by analyzing temporal sections at the zero-crossings of the d- and g-type wave functions. Both methods for analysis were experimentally verified in a pump-probe experiment with bichromatic COCP pulse sequences to exclusively excite Rydberg f states, probed into the g-type continuum.

In general, the experiments presented in this paper demonstrate the capability of our bichromatic polarization pulse shaping scheme to precisely generate phase-locked bichromatic polarization-shaped pulse sequences for background-free pump-probe studies on ultrafast dynamics. Due to the octave-spanning white light input spectrum, a wide range of continuously tunable wavelengths is accessible. Since all bichromatic field parameters are adjustable, the bichromatic fields can be adapted to the physical system under investigation. For example, the frequency of both pulses in the sequence can be tuned precisely to either excite or avoid atomic resonances. In multiphoton processes, the tunability can be used in addition to control multiphoton interferences of different order. Specific pathways can be selected via the polarization state of the pump and the probe pulse. Finally, accurate control over the pulse duration and the time delay allows us to adapt the sequence to follow the system's dynamics. Therefore, the shaper-based pump-probe technique opens up new experimental opportunities for time-resolved polarization-sensitive multicolor studies in many research fields. Initial applications of the shaping scheme have already been demonstrated on intrapulse frequency-mixing from perturbative $1 + 2$ resonance-enhanced multiphoton ionization of K atoms [24] and on carrier-envelope phase (CEP) control of spatial asymmetries in the photoemission from MPI of xenon atoms [21]. Building on the results presented in this paper, we plan to carry out pump-probe studies with shaper-generated multicolor laser pulse sequences. For example, commensurable bichromatic pump pulses will be used to excite CEP-sensitive Rydberg wave packets with angular precession from the interference of states with opposite parity, ionized via a probe pulse of third color. Currently, we study a pump-probe scheme similar to [18,39] to create a reference wave packet for holographic reconstruction of the amplitude and phase of Rydberg wave packets.

ACKNOWLEDGMENTS

Financial support by the Deutsche Forschungsgemeinschaft via the priority programme SPP1840 QUTIF is gratefully acknowledged.

[1] T. Gallagher, *Rydberg Atoms* (Cambridge University Press, Cambridge, England, 2005), Vol. 3.
[2] K. Ohmori, Annu. Rev. Phys. Chem. **60**, 487 (2009).
[3] G. Alber and P. Zoller, Phys. Rep. **199**, 231 (1991).
[4] G. Alber, H. Ritsch, and P. Zoller, Phys. Rev. A **34**, 1058 (1986).
[5] L. Noordam and R. Jones, J. Mod. Opt. **44**, 2515 (1997).
[6] R. Carley, E. Boleat, R. Minns, R. Patel, and H. Fielding, J. Phys. B **38**, 1907 (2005).
[7] L. D. Noordam, D. I. Duncan, and T. F. Gallagher, Phys. Rev. A **45**, 4734 (1992).
[8] R. Jones and L. Noordam, Adv. At., Mol., Opt. Phys. **38**, 1 (1998).
[9] J. Ahn, Science **287**, 463 (2000).
[10] J. Ahn, C. Rangan, D. N. Hutchinson, and P. H. Bucksbaum, Phys. Rev. A **66**, 022312 (2002).
[11] M. Saffman, J. Phys. B **49**, 202001 (2016).
[12] H. Weimer, M. Müller, I. Lesanovsky, P. Zoller, and H. P. Büchler, Nat. Phys. **6**, 382 (2010).
[13] M. Aymar, E. Luc-Koenig, and F. C. Farnoux, J. Phys. B **9**, 1279 (1976).
[14] D. W. Schumacher, J. H. Hoogenraad, D. Pinkos, and P. H. Bucksbaum, Phys. Rev. A **52**, 4719 (1995).
[15] A. ten Wolde, L. D. Noordam, A. Lagendijk, and H. B. van Linden van den Heuvell, Phys. Rev. Lett. **61**, 2099 (1988).
[16] J. Mauritsson, T. Remetter, M. Swoboda, K. Klünder, A. L'Huillier, K. J. Schafer, O. Ghafur, F. Kelkensberg, W. Siu, P. Johnsson, M. J. J. Vrakking, I. Znakovskaya, T. Uphues, S. Zherebtsov, M. F. Kling, F. Lépine, E. Benedetti, F. Ferrari, G. Sansone, and M. Nisoli, Phys. Rev. Lett. **105**, 053001 (2010).
[17] J. Verlet and H. Fielding, Int. Rev. Phys. Chem. **20**, 283 (2001).
[18] T. C. Weinacht, J. Ahn, and P. H. Bucksbaum, Nature **397**, 233 (1999).
[19] T. C. Weinacht, J. Ahn, and P. H. Bucksbaum, Phys. Rev. Lett. **80**, 5508 (1998).
[20] H. Fielding, Annu. Rev. Phys. Chem. **56**, 91 (2005).
[21] S. Kerbstadt, D. Pengel, L. Englert, T. Bayer, and M. Wollenhaupt, Phys. Rev. A **97**, 063402 (2018).
[22] S. Kerbstadt, L. Englert, T. Bayer, and M. Wollenhaupt, J. Mod. Opt. **64**, 1010 (2017).
[23] S. Kerbstadt, D. Timmer, L. Englert, T. Bayer, and M. Wollenhaupt, Opt. Express **25**, 12518 (2017).
[24] S. Kerbstadt, D. Pengel, D. Johannmeyer, L. Englert, T. Bayer, and M. Wollenhaupt, New J. Phys. **19**, 103017 (2017).
[25] J. Köhler, M. Wollenhaupt, T. Bayer, C. Sarpe, and T. Baumert, Opt. Express **19**, 11638 (2011).
[26] A. T. J. B. Eppink and D. H. Parker, Rev. Sci. Instrum. **68**, 3477 (1997).
[27] T. Brixner and G. Gerber, Opt. Lett. **26**, 557 (2001).
[28] A. M. Weiner, Opt. Comm. **284**, 3669 (2011).
[29] T. Baumert, T. Brixner, V. Seyfried, M. Strehle, and G. Gerber, Appl. Phys. B **65**, 779 (1997).
[30] D. Yelin, D. Meshulach, and Y. Silberberg, Opt. Lett. **22**, 1793 (1997).
[31] G. A. Garcia, L. Nahon, and I. Powis, Rev. Sci. Instrum. **75**, 4989 (2004).
[32] A. Wituschek, J. von Vangerow, J. Grzesiak, F. Stienkemeier, and M. Mudrich, Rev. Sci. Instrum. **87**, 083105 (2016).
[33] M. Krug, T. Bayer, M. Wollenhaupt, C. Sarpe-Tudoran, T. Baumert, S. S. Ivanov, and N. V. Vitanov, New J. Phys. **11**, 105051 (2009).
[34] J. Parker and C. R. Stroud, Jr., Phys. Rev. Lett. **56**, 716 (1986).
[35] M. Wollenhaupt, M. Krug, J. Köhler, T. Bayer, C. Sarpe-Tudoran, and T. Baumert, Appl. Phys. B **95**, 245 (2009).
[36] A. Kramida, Y. Ralchenko, and J. Reader, NIST ASD Team NIST Atomic Spectra Database (version 5.5. 6) (2018).
[37] M. Shapiro and P. Brumer, *Principles of the Quantum Control of Molecular Processes* (John Wiley and Sons, Hoboken, NJ, 2003), Vol. 1.
[38] P. Hockett, M. Wollenhaupt, C. Lux, and T. Baumert, Phys. Rev. Lett. **112**, 223001 (2014).
[39] D. M. Villeneuve, P. Hockett, M. J. J. Vrakking, and H. Niikura, Science **356**, 1150 (2017).